

Selection of carbon nanotubes with specific chiralities using helical assemblies of flavin mononucleotide

SANG-YONG JU¹, JONATHAN DOLL¹, ITY SHARMA² AND FOTIOS PAPADIMITRAKOPOULOS^{1,2*}

¹Nanomaterials Optoelectronics Laboratory (NOEL), Polymer Program, University of Connecticut, Storrs, Connecticut 06269-3136, USA

²Department of Chemistry, Institute of Materials Science, University of Connecticut, Storrs, Connecticut 06269-3136, USA

*e-mail: papadim@mail.ims.uconn.edu

Published online: 30 May 2008; doi:10.1038/nano.2008.148

The chirality of single-walled carbon nanotubes affects many of their physical and electronic properties. Current production methods result in nanotubes of mixed chiralities, so facile extraction of specific chiralities of single-walled carbon nanotubes is an important step in their effective utilization. Here we show that the flavin mononucleotide, a common redox cofactor, wraps around single-walled carbon nanotubes in a helical pattern that imparts efficient individualization and chirality selection. The cooperative hydrogen bonding between adjacent flavin moieties results in the formation of a helical ribbon, which organizes around single-walled carbon nanotubes through concentric π - π interactions between the flavin mononucleotide and the underlying graphene wall. The strength of the helical flavin mononucleotide assembly is strongly dependent on nanotube chirality. In the presence of a surfactant, the flavin mononucleotide assembly is disrupted and replaced without precipitation by a surfactant micelle. The significantly higher affinity of the flavin mononucleotide assembly for (8,6)-single-walled carbon nanotubes results in an 85% chirality enrichment from a nanotube sample with broad diameter distribution.

The presence of multiple (n,m) chirality single-walled carbon nanotubes (SWNTs) in a given sample poses a major barrier towards realizing the exceptional electronic and mechanical properties of these nanostructured materials in high-end applications^{1,2}. Recent studies have shown that the organization of specialized surfactants onto nanotubes has been able to impart selective enrichment of a few particular (n,m)-SWNTs³⁻⁷. The key motif for such (n,m) enrichment hinges on π - π interactions between the underlying graphene sidewall and the aromatic moieties of these surfactants. This is augmented by the attachment of solvent-interacting groups to these aromatic moieties to prevent nanotube aggregation, allowing the surfactant to uninterruptedly organize around the nanotube. The two-dimensional (2D) sidewall organization of these aromatic moieties into a wrapping sheath and its interaction with the underlying (n,m) chirality, appears to be crucial for the selective (n,m) enrichment².

Such a paradigm departure from all other SWNT separation schemes⁸⁻¹² was first inferred by DNA wrapping, which afforded nanotube enrichment according to type (metallic versus semiconducting)^{3,4}, diameter⁴ and (n,m) chirality¹³. This was followed by the application of polyfluorenes (PFO), where variation in their chemical motifs resulted in the enrichment of selective (n,m) nanotubes^{5,6}. Both DNA and PFO methodologies make use of the initial organization of π -interacting chromophores into a one-dimensional (1D) chain, which first adsorbs and then organizes into 2D sheaths around the nanotube sidewalls. The polymeric nature of DNA and PFO surfactants, however, hinders post-separation surfactant removal, which is necessary to enable the (n,m)-selected nanotube to be recovered

in its pristine form. In this article, we describe the 1D organization of flavin moiety into helical ribbons that wrap around SWNTs of a narrow diameter range. The adhesion of these flavin ribbons appear to be (n,m)-dependent, and they can be readily exchanged by an aliphatic-tail surfactant that is easily removed to yield pristine nanotube samples. Moreover, the particular affinity of these flavin ribbons towards (8,6)-SWNTs allows the selective enrichment of a single chirality by means of a salting-out precipitation process.

Flavin mononucleotide (FMN; Fig. 1d inset) is the phosphorylated form of vitamin B₂ and is a well-known redox cofactor to a number of oxidoreductase proteins¹⁴. This readily available chemical consists of an aromatic isoalloxazine moiety and a chiral *d*-ribityl phosphate group. Flavin adenine dinucleotide (FAD), the redox cofactor of glucose oxidase (GOx), which shares the entire FMN moiety, has been shown to spontaneously adsorb onto nanotubes and facilitate quasi-reversible electron transfer with SWNT electrodes¹⁵. The covalent attachment of FAD to SWNTs followed by its subsequent re-constitution with the *apo*-GOx enzyme has shown the highest electron turnover rate in a glucose sensing configuration¹⁶. A recent theoretical study indicates that the isoalloxazine moiety of FAD forms π - π interactions with SWNTs and results in redshift of carbon nanotube photoluminescence (PL)¹⁷. This was independently confirmed by a recent report indicating that SWNT-attached FMN collapses on the sidewalls due to a profound isoalloxazine-nanotube interaction¹⁸. This finding has prompted us to investigate FMN as a nanotube de-bundling agent. Surprisingly, simple sonication of a mixture of 1 mg HiPco-SWNTs, 4 mg FMN and 4 ml D₂O (see Methods), followed by centrifugation at

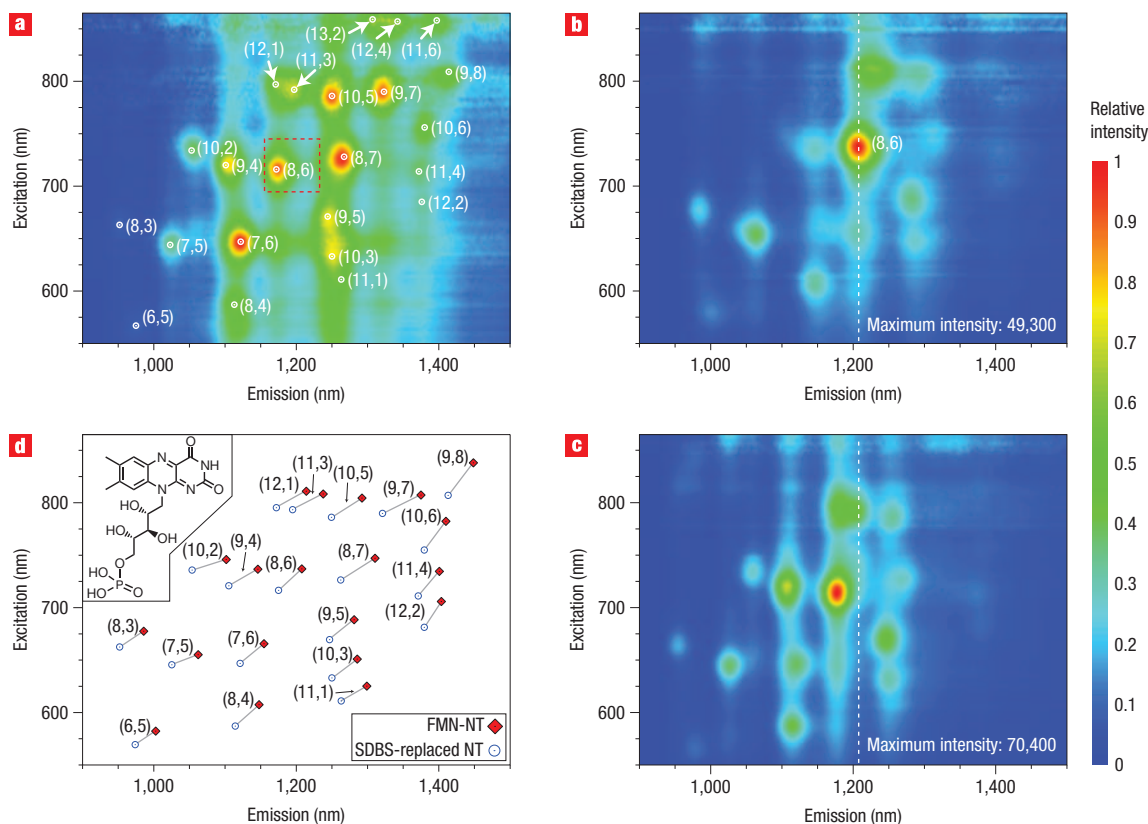


Figure 1 Photoluminescence emission (PLE) maps of HiPco-SWNT samples. **a, b**, Maps of HiPco-SWNT samples dispersed with SDBS and centrifuged at 200,000g (**a**) and dispersed with FMN and centrifuged at 15,000g (**b**). **c**, Sample **b** after the addition of 7.4 mM SDBS. **d**, Plot of E_{11}^S and E_{22}^S transitions for FMN (red diamonds) and SDBS (blue circles) dispersed SWNTs. The inset in **d** illustrates the chemical structure of FMN.

15,000g resulted in a clear greenish-dark dispersion that exhibited a well-resolved PL excitation (PLE) map (Fig. 1b).

Figure 1a shows the PLE map of the starting HiPco nanotube sample dispersed in sodium dodecyl benzene sulphonate (SDBS). The map reveals the presence of 26 different semiconducting (n,m) chirality nanotubes with a diameter (d_t) distribution spanning from 0.76 to 1.24 nm (ref. 19). The plot of PL intensity versus d_t (see Supplementary Information, Fig. S1a) from all nanotube chiralities shown in Fig. 1a conforms to a broad unimodal abundance profile, as previously reported¹⁹. Figure 1b depicts the PLE map of the same HiPco sample dispersed in FMN. Besides the profound narrowing in diameter distribution (0.76–1.17 nm), the (8,6)-SWNT appears to be significantly enriched (from 5 to 17%, based on the relative intensity from Fig. 1a,b, respectively). This d_t narrowing originates from the exclusion of large d_t nanotubes (from 1.17 to 1.27 nm), belonging mainly to families ($2n + m = \text{constant}$) 26 and 28. If the strong (8,6)-SWNT is temporarily neglected, the remaining PL intensity versus d_t plot of Fig. S1b (see Supplementary Information) appears to exhibit a bimodal distribution (see Supplementary Information, Fig. S1b, green curves).

Such a distribution indicates that, apart from narrowing the diameter distribution of the starting SWNT sample (Fig. 1a), other factors might be involved. To verify this hypothesis, we added 7.4 mM of SDBS in the FMN/SWNT dispersion of Fig. 1b, shook the suspension by hand, and re-acquired the PLE map, as shown in Fig. 1c. The addition of SDBS did not disturb the nanotube suspension, although it resulted in profound changes in terms of peak positions, relative PL intensities and

maximum PL intensity values, readily seen by comparing Fig. 1b,c. Moreover, the plot of PL intensity versus d_t (see Supplementary Information, Fig. S1c) regained its unimodal distribution. In addition, the relative PL intensity of the (8,6)-SWNT was slightly lowered with respect to the rest of the remaining nanotubes, from 17 to 15%. This presents convincing evidence that the diameter distribution narrowing is real, but the interaction of nanotubes with the isoalloxazine moiety of FMN results in partial quenching of their PL intensity. This statement is further substantiated by the change in maximum PL intensity (from 49,300 counts in Fig. 1b to 70,400 counts in Fig. 1c) and the observed redshift for all nanotubes (see dotted line for (8,6)) in the presence of FMN only.

Figure 1d illustrates the magnitude of the FMN-induced redshift on both the first (E_{11}^S) and second (E_{22}^S) optical transitions of semiconducting SWNTs. These values span from 15 to 51 meV and 23 to 71 meV for E_{11}^S and E_{22}^S , respectively. (See Supplementary Information, Table S1, for an analytical account of PLE-derived peak positions, full-width at half-maximum (FWHM) and relative PL intensity for Fig. 1a–c.) Upon closer inspection of these results, it becomes apparent that the magnitude of redshifts, FWHM and %PL quenching display a complex pattern for all the investigated nanotubes. This pattern does not obey the diameter-driven PL quenching previously reported for nanotubes in the presence of redox reagents and aromatic charge transfer (CT) agents (TTF, TCNQ, and so on)^{20,21}.

Such a complex pattern may arise from the potential organization of isoalloxazine on the graphene sidewalls. Unlike TTF and TCNQ, which do not possess self-interacting groups, the

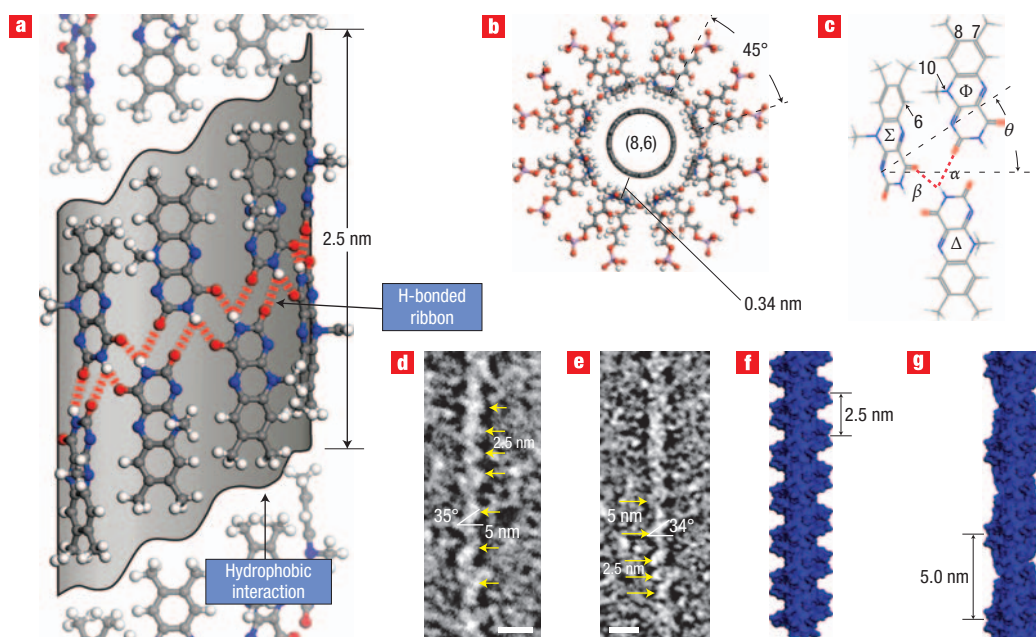


Figure 2 Helical wrapping motif of FMN around SWNTs. **a**, Top view of isoalloxazine moieties wrapped in an δ_1 helical pattern. The helical ribbon (shaded structure) is stabilized by (i) four H bonds (red dashed lines) between adjacent isoalloxazine moieties and (ii) charge transfer interactions with the underlying graphene side walls. **b**, The long *d*-ribityl phosphate side groups of FMN provide aqueous solubilization. **c**, Hydrogen bonding (α and β) and steric (6 and 10 positions) considerations of the helical repeat pair (that is, (Φ/Δ) or (Δ/Σ)). Angle θ is the projected pitch angle. **d,e**, Representative HRTEM images of uranyl acetate stained FMN-wrapped SWNTs. Scale bars, 5 nm. Yellow arrows indicate the periodic maxima of the uranyl acetate staining patterns. **f,g**, Simulated FMN helical configurations, where the *d*-ribityl phosphate moieties are collapsed in groups of two and four side chains, respectively.

uracil moiety of isoalloxazine is capable of self-assembly into ribbons (Fig. 2a) by means of intermolecular hydrogen bonding (H bonding). The driving force for such ribbon formation appears to originate from (i) the concentric π - π interaction between the isoalloxazine ring and the graphene sidewall of SWNT¹⁷ (Fig. 2b) and (ii) the quadruple H bonding between opposing isoalloxazine moieties, shown as red broken lines in Fig. 2a. The basic repeat for the formation of this ribbon is either Σ/Δ or Φ/Δ isoalloxazine pairs (Fig. 2c) in an δ_1 helical pattern, where the long axis of the isoalloxazine rings aligns with the nanotube axis. Such an arrangement produces a seamless tubular structure with diameter of 1.65 nm and a projected pitch angle θ of 34° , which provides an ideal encasement for (8,6)-SWNT ($d_{t,(8,6)} = 0.97$ nm) with 0.34 nm van der Waals spacing, similar to that of the 'ABAB' stacking of graphite¹ ($0.97 + 2 \times 0.34 = 1.65$ nm).

Figure 2c represents a schematic illustration of isoalloxazine repeat-induced diameter selectivity in SWNTs. The formation of the helix is strongly dependent on the H bond strength of α and β pairs versus the van der Waals repulsion between Σ and Φ isoalloxazine moieties, concentrated mainly on the adjacent 6Σ -H and 10Φ -CH₃ groups. Two organization extremes have been investigated based on a fixed δ_1 helix and a variable pitch u_t helix, where u/t approaches a value of 8. In the case of the fixed δ_1 helix, expansion or shrinkage of the tubular diameter is directly controlled by the β H bonding distance. Assuming that the optimum H bonding distance (H...O) varies from 0.18 to 0.26 nm, the tubular diameter ranges from 1.45 to 1.75 nm. By subtracting the optimum van der Waals distance (0.34 nm), the tubular inclusion range varies from 0.77 to 1.07 nm, which is in agreement with the major d_t distribution shown in Fig. S1c (see Supplementary Information; 0.76–1.17 nm). In the case of the variable u_t helix, the decrease in the projected pitch angle θ

(Fig. 2c) brings closer the 6Σ -H and 10Φ -CH₃ moieties, pushing further the neighbouring Σ and Φ isoalloxazine groups. This in turn increases tube diameter at the cost of weakening α and β H bonding pairs. This provides a qualitative explanation as to why large-diameter helices become less energetically favourable. A more quantitative approach considering 'pitch-induced' packing of the 7- and 8-CH₃ groups of neighbouring ribbons (Fig. 2a), localized π - π interactions of flavin with nanotube, and finite isoalloxazine misalignment from the long nanotube axis to better accommodate the underlying chiral graphene pattern is presently under investigation.

High-resolution transmission electron microscopy (HRTEM) was used to confirm FMN helical wrapping around SWNTs. Figure 2d,e illustrates two representative HRTEM images of uranyl acetate stained FMN/HiPco-SWNTs (see Methods). Helical patterns around individualized SWNTs that extend for over 300 nm are clearly evident (see Supplementary Information, Fig. S2a–f, for more images). The periodic undulation of uranyl acetate staining patterns occurs every 2.5 ± 0.4 or 5.0 ± 0.4 nm along the SWNTs (between the yellow arrows in Fig. 2d,e), with a projected pitch angle varying between 34 and 37° . These undulations are expected to originate from the collapsed *d*-ribityl phosphate side chains of FMN shown in Fig. 2b. Upon drying, these side chains can collapse with their nearest neighbour, producing a nanotube profile of a 2.5-nm periodicity as shown in a simulated profile in Fig. 2f. The considerably greater length of the *d*-ribityl phosphate groups (1.15 nm) with respect to the long axis of the isoalloxazine ring (1.0 nm) can, however, lead to a collapse of four side groups into a single feature, as simulated in Fig. 2g, resulting in a 5-nm spacing (also observed in Fig. 2d,e). Both configurations show a projected pitch angle of $\sim 35^\circ$, which is in good agreement with $\theta = 34^\circ$ for the δ_1 helix in Fig. 2c.

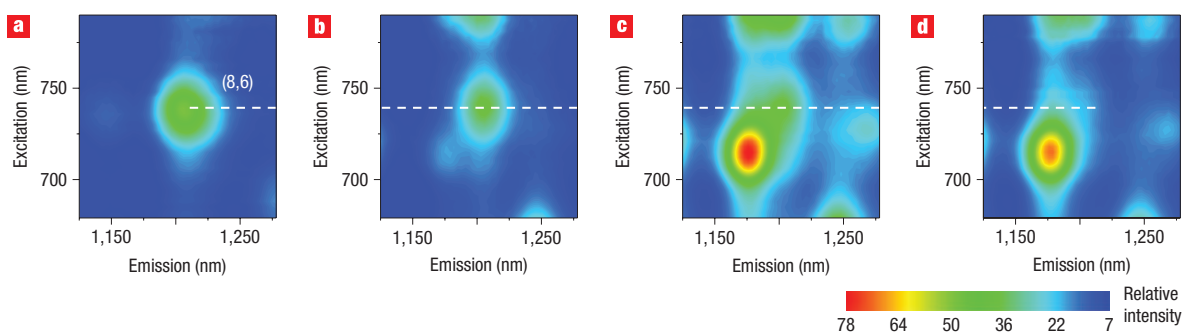


Figure 3 PLE-assisted determination of FMN replacement by SDBS titration, zooming on (8,6)-SWNT. **a–d**, PLE maps of FMN-dispersed nanotubes upon addition of 0 (**a**), 2.3 (**b**), 4.3 (**c**) and 7.4 mM (**d**) SDBS. The dotted line allows visualization of the gradual blueshift of the emission from (8,6)-SWNTs as FMN is replaced by SDBS. This blueshift on addition of SDBS can be used to quantify the affinity of FMN for different chirality SWNTs.

To establish the selective affinity of the FMN helix on different chirality nanotubes, PLE mapping of FMN-dispersed SWNTs was collected at varying SDBS concentrations. Figure 3a–d presents a PLE close-up image of the progressive blueshift of the (8,6) nanotube for increasing addition of SDBS. Figure 3b shows an easily resolvable peak and shoulder for FMN and SDBS positions, respectively, and Fig. 3c has these features reversed. (See Supplementary Information, Fig. S3 and Table S2, for the PL intensities for all resolvable nanotubes as a function of SDBS concentration.)

Figure 4a–c illustrates the SDBS PL intensity versus SDBS concentration for (8,6)-, (9,4)- and (8,3)-SWNTs, respectively. The sharp sigmoidal onset varies from nanotube to nanotube, as shown in Fig. 4a–c (see also Supplementary Information, Table S2, and elsewhere). The relative FMN-wrapping affinity (K_a) against SDBS replacement has been derived using the Hill equation²² (fitted red curve in Fig. 4a–c; see also Supplementary Information, Table S2, for the affinity given in terms of SDBS mM concentration). No PLE is observed in the SDBS position for concentrations below the SDBS critical micelle concentration (CMC), which, in the presence of SWNTs, is estimated at 1 mM (ref. 23). This indicates that the micellar organization of SDBS is vital for FMN replacement. With the exception of (8,6)-SWNT, the onset of SDBS replacement for these nanotubes starts very close to the SDBS CMC concentration (Fig. 4a–c; see also Supplementary Information, Table S2). The much stronger FMN affinity for (8,6)-SWNT provides an explanation for the apparent enrichment in Fig. 1b,c.

Although the aforementioned K_a affinity of FMN to various chirality SWNTs addresses the relative strength of the FMN helix against SDBS, it leaves unanswered the complex PL redshift pattern of Fig. 1d. Figure 5 illustrates the plot of chiral angle against E_{11}^S red shift of Fig. 1d (see Supplementary Information, Fig. S4, for the corresponding E_{22}^S red shift). When each (n,m) nanotube is linked to its own $(2n+m = \text{constant})$ family, a complex zigzag pattern arises. Upon closer investigation of Fig. 5, the $\text{mod}[(n-m)/3] = 1$ nanotube families (26, 23 and 20) exhibit correspondingly less redshift compared to $\text{mod} = 2$ families (25, 22 and 19). This trend is reversed for the E_{22}^S plot of Fig. S4 (see Supplementary Information). Although the nature of this complex pattern is not currently known, the underlying zigzag pattern resembling an odd–even effect suggests that the FMN helix forms around all the nanotubes interrogated in Fig. 1b. Such an odd–even effect has been observed in many organization patterns of surfactants and liquid crystals with varying $(-\text{CH}_2-)_n$

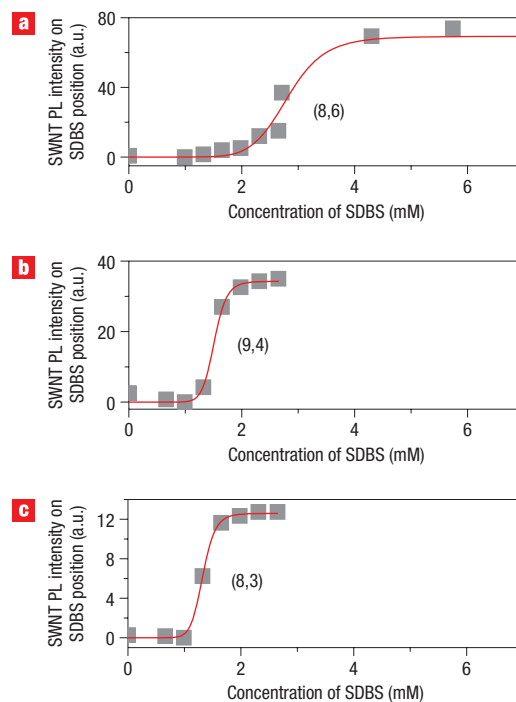


Figure 4 Chirality-dependent affinity of FMN-wrapped SWNTs, as determined by SDBS titration. **a–c**, SDBS-derived PL intensity profiles for (8,6)- (**a**), (9,4)- (**b**) and (8,3)-SWNTs (**c**) as a function of SDBS concentration. Red curves are based on Hill equation fitting (see Methods). The inflection occurs close to the critical micelle concentration (CMC) of SDBS for both (9,4)- and (8,3)-SWNTs. For (8,6)-SWNTs the inflection occurs at a concentration well above the CMC; this offers an explanation for the selective enrichment that is observed.

chain lengths and is known to profoundly effect packing and molecular structure in the vicinity of ordered surfaces²⁴.

The substantial K_a affinity of (8,6)-SWNT for the FMN helix ($K_a = 2.8$) versus that of the remaining chiralities ($1.2 < K_a < 2.1$) (Fig. 4a–c; see also Supplementary Information, Table S2), encouraged us to investigate conditions that selectively enrich the (8,6) nanotube. In accordance with the aforementioned K_a , the introduction of 2.65 mM SDBS should replace the FMN helices

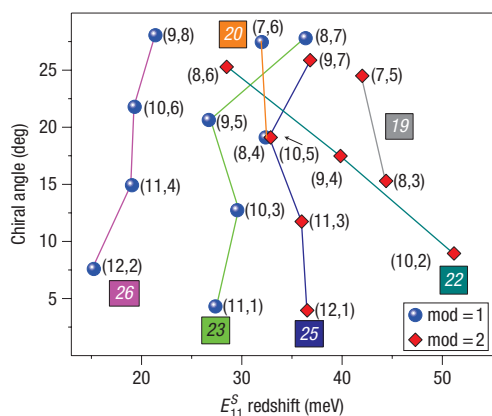


Figure 5 Chirality, family and modality dependence of FMN-induced E_{11}^S redshift for all PLE-observed nanotubes. Interpolated zigzag lines follow distinct colour-coded family ($2n + m = \text{constant}$) and modality ($\text{mod} = 1$ or 2) patterns.

in all but the (8,6)-SWNT. It has been reported²⁵ that the addition of NaCl can precipitate sodium dodecyl sulphate (SDS) suspended SWNTs. In the case of FMN, we observed little or no precipitation of FMN-wrapped SWNTs even after the addition of up to 0.714 M NaCl (see Supplementary Information, Fig. S5). Based on the different ionic stability of SDBS (sulphate) versus FMN (phosphate) suspended SWNTs, 0.5 M NaCl was added to the 2.65 mM SDBS-containing FMN suspension, which caused a massive flocculation of SWNTs. Following a 10-min, 13,000g centrifugation step, the supernatant was recovered and investigated using PLE and UV-vis-NIR spectroscopy, shown in Fig. 6a,b, respectively. The dramatic enrichment of (8,6)-SWNT is evident in both figures. By comparing the maximum PL intensity in Fig. 1b and Fig. 6a, 76% of (8,6) nanotubes are retained in the supernatant.

Although the visualization of nanotubes other than (8,6) and its phonon modes²⁶ is difficult from Fig. 6a, a baseline close-up (see Supplementary Information, Fig. S6) indicates that the (9,5) nanotube is also present. The optical absorption of Fig. 6b agrees with the profound enrichment of (8,6) at 1,203 nm, along with the small presence of (9,5) at 1,278 nm. The profound absorption upswing at wavelengths below 800 nm is mostly attributed to the tail-end absorption of FMN (0.1 wt%), and to a lesser extent to residual scattering of SDBS micelles and the presence of amorphous carbon. Although the K_a of (9,5) is significantly less than that of (8,6), the fact that both nanotube species have similar diameters (0.97 and 0.98 nm for (8,6) and (9,5), respectively) suggests that during SDBS/salt flocculation, (9,5) is re-wrapped by FMN, and remains in solution. The enrichment factor for (8,6) was estimated at 85% based on both PLE and UV-vis-NIR spectroscopy (see Methods and Supplementary Information). To the best of our knowledge, this presents the simplest, chirality-specific enrichment methodology ever reported, from a broad d_t nanotube sample as HiPco. Fine-tuning of this methodology along with repetitive cycling is expected to further increase the enrichment factor for (8,6)-SWNTs.

In summary, the readily available, low-molecular-weight, H bonding prone, flavin mononucleotide (FMN) has been used to disperse and individualize HiPco-SWNTs. This dispersion is based on helical FMN wrapping around SWNTs, causing a unique redshift pattern as a result of the interaction of the helical isoalloxazine assembly with the underlying nanotube chirality.

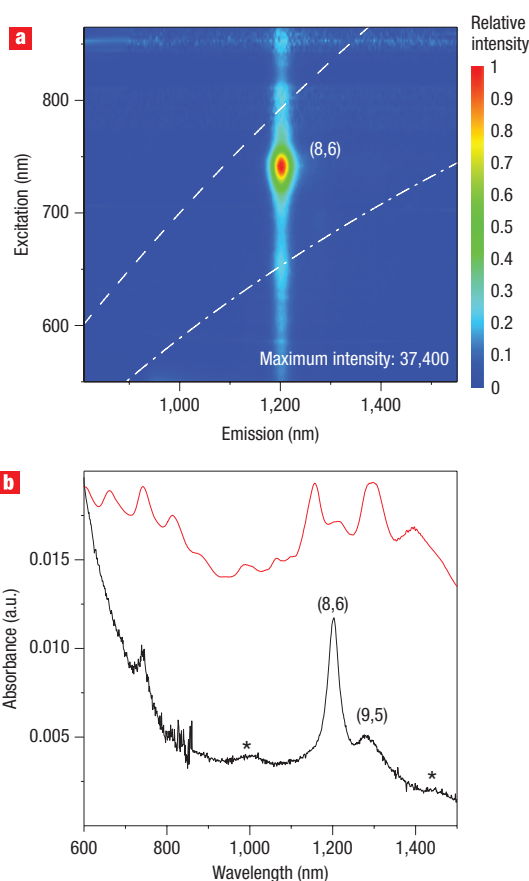


Figure 6 Enrichment of the (8,6) nanotube using (i) selective SDBS replacement of FMN on all but (8,6)-SWNTs, and (ii) addition of NaCl to salt out all SDBS-dispersed nanotubes. **a**, PLE map of the (8,6) nanotube in the salt-out supernatant. Broken white lines indicate two carbon nanotube phonon modes. **b**, UV-vis-NIR spectra of the corresponding salt-out supernatant (black solid line), compared with the initial FMN-dispersed HiPco sample (red solid line). The upper (red) spectra in **b** was multiplied by 0.05 and offset upwards by 0.01 absorbance units to facilitate visual comparison. The asterisks denote phonon mode absorption of the (8,6)-SWNT (ref. 13).

For reasons not yet established, (8,6)-SWNTs show profound affinity for the FMN helix. This was used for the selective enrichment of the (8,6) nanotubes (85% enrichment value), using a simple surfactant replacement and subsequent salting-out precipitation. Variations in the structure of isoalloxazine and its pendant side group are expected to lead to enrichment of nanotubes of different (n,m) chiralities. This generic and highly flexible enrichment methodology, using the biologically relevant FMN redox cofactor, is poised to provide further impetus for the separation and derivatization of SWNTs, with broad applicability to biosensory, drug and gene delivery, as well as optoelectronics and electro-optic device applications.

METHODS

MATERIALS

FMN and SDBS were purchased from Aldrich. Deuterated water (D_2O) was purchased from Acros and used as received. SWNTs were prepared by a high-pressure carbon monoxide process (HiPco, Lot P0339, with diameter (d_t) distribution 1.00 ± 0.35 nm) as obtained by Carbon Nanotechnologies Inc. (CNI)²⁷. Precautions were taken to avoid prolonged exposure of FMN to direct

sunlight by carrying the experiments in a laboratory equipped with yellow lights. Fluorescence spectroscopy measurements were conducted on a Jobin-Yvon Spex Fluorolog 3-211 spectrofluorometer equipped with a PMT NIR detector with 3-nm step size in both excitation and emission wavelengths. Both excitation and emission light intensities were corrected against instrumental variations using Spex Fluorolog sensitivity correction factors. The UV-vis-NIR absorption spectra were measured with a Perkin-Elmer Lambda 900 UV-vis-NIR spectrometer. TEM measurements were performed using a JEOL JEM-2010 electron microscope operating at 200 kV.

DISPERSION AND TITRATION METHOD

SDBS–HiPco suspension protocol (sample a). A mixture of 1 mg HiPco–SWNT and 1 wt% SDBS was added to 4 ml D₂O, according to the literature²⁸. The solution was homogenized for 1 h, followed by sonication for 10 min at 600 W intensity. The resulting solution was centrifuged at 200,000g for 2 h and the supernatant (upper 80%) was collected to produce a clear dark solution.

FMN–HiPco suspension protocol (sample b). A mixture of 1 mg HiPco–SWNT and 4 mg FMN was added to 4 ml D₂O. The solution was sonicated for 4 h at 300 W intensity. The resulting greenish-dark solution was centrifuged at 15,000g for 2 h and the supernatant (decanted from the upper 90% suspension) was carefully collected, to remove any bundled carbon nanotubes, to produce a clear greenish-dark solution.

Titration of SDBS into FMN–HiPco suspension. Microlitre portions of 50 mM SDBS–D₂O stock solution were added to sample b in order to obtain the desired SDBS concentration. This solution was gently hand-shaken to prevent any bubble formation and characterized spectroscopically without exposure to sonication or ambient light. Sample c contained 7.4 mM SDBS.

MOLECULAR MODELLING

Cerius2 simulation software was used for molecular modelling using the Dreiding 2.21 force field for molecular mechanics, molecular dynamics and quenched dynamics simulations. The charge equilibration method was used to set atom charges for FMN, and zero charge was assigned for all SWNT carbon atoms. Materials Studio 4 software was used for visualization. An *sp*³ geometry was used for the N atom at the 10 position of the isoalloxazine ring (Fig. 2c), whereas for the rest of the aromatic atoms an *sp*² configuration was used. Molecular mechanics and quenched molecular dynamics within periodic boundary condition were used to relax the constructed helices and optimize $\Sigma/\Phi/\Delta$ FMN trimer conformations (Fig. 2c). The 8₁ FMN helix of Fig. 2a,b was constructed based on the *I*4₁/*a* 2/*m* 2/*d* (D_{4h}¹⁹) no. 141 space group, using the Φ/Δ FMN dimer as a repeat. By adjusting the spatial arrangement of Φ and Δ isoalloxazine units in the dimer repeat, helices with different diameters and pitches were generated, and subsequently optimized, within the aforementioned space group. For helices other than 8₁, the FMN trimer with preset intermolecular angles was used, followed by subsequent optimization under periodic boundary conditions.

PREPARATION OF THE FMN–HIPCO SAMPLE FOR TEM MEASUREMENT

TEM specimens were prepared according to the literature²⁹. The TEM grids used were covered with an ultrathin carbon support film on a lacey carbon support (Ted Pella). All grids were made hydrophilic before sample deposition by exposing them to high-intensity UV light. The 15,000g centrifuged FMN–HiPco sample was diluted ($\times 100$), and 5 μ l was drop cast onto the TEM grid. After 2 min of incubation, the excess sample was carefully wicked off from the grid using a filter paper. After two washes with 5 μ l water, 3 μ l of 1% uranyl acetate solution was added to the sample and allowed to incubate for 1 min before the excess was wicked off with filter paper, and dried.

RELATIVE AFFINITY (K_a) OF FMN–SWNT WRAPPING AGAINST SDBS CONCENTRATION

Figure 4a–c shows the sigmoidal relationship of PL intensity profile versus SDBS concentration ([SDBS]). The sigmoidal profiles were fit using the Hill equation²²:

$$\rho = \frac{[\text{SDBS}]^\gamma}{[K_a]^\gamma + [\text{SDBS}]^\gamma} \quad (1)$$

where ρ is PL intensity measured at the SDBS position of each nanotube, K_a denotes a relative affinity of FMN–SWNT to SDBS for producing half of the PL intensity of the specific (*n,m*) carbon nanotube at the SDBS position (see Supplementary Information, Table S2), and γ is the fitted Hill coefficient describing the breadth of the sigmoidal transition. The relative K_a affinities for all

nanotubes span between 1.3 and 2.8 mM of SDBS (see Supplementary Information, Table S2). Among these nanotubes, (8,6) and (7,5) nanotubes show the highest (2.8 mM) and lowest (1.2 mM) K_a values, respectively. The observed γ values span from 3 to 16. Such high γ values imply that SDBS rapidly replaces the FMN helix, presumably by unzipping the H-bonded isoalloxazine ribbon wrapped around these carbon nanotubes.

(8,6) ENRICHMENT PROTOCOL

Following the addition of 2.65 mM SDBS in sample b, the greenish-dark nanotube solution was gently hand-shaken. The local PLE maps (excitation and emission ranging from 679 to 790 nm and 1,125 to 1,278 nm, respectively) were taken to ensure that all but (8,6) FMN-dispersed nanotubes have been replaced with SDBS. Then, 0.5 M NaCl was added, hand-shaken and quickly centrifuged at 13,000g for 10 min, keeping only the supernatant.

UV-VIS-NIR-CALCULATED ENRICHMENT FACTORS

As shown in Fig. S7 (see Supplementary Information), deconvolution of the UV-vis-NIR spectrum illustrates that the enrichment factors of (8,6) and (9,5) nanotubes are 85 and 15%, respectively, assuming they both exhibit similar extinction coefficients. The latter assumption is close to the theoretically calculated relative absorbance difference of 2.18 and 1.88 for both (8,6) and (9,5), respectively³⁰. Using these values, the enrichment factors shift to 83 and 17%, respectively.

PLE-CALCULATED ENRICHMENT FACTORS

As shown in Fig. S6 (see Supplementary Information), the PL intensity for (8,6) and (9,5) are estimated to be 1 and 0.069 arbitrary units, respectively. Using the calculated PL quantum efficiencies by Oyama *et al.*³⁰ (0.49 and 0.28 for (8,6) and (9,5), respectively) and taking into account the relative %PL quenching induced by FMN (0.31 and 0.47 for (8,6) and (9,5), respectively; see Supplementary Information, Table S1), the PLE enrichment factors were calculated to be 86 and 14%, respectively. These values are in good agreement with the UV-vis-NIR enrichment values determined above. The mean average of all three estimates provided enrichment values of 85 and 15% for (8,6)- and (9,5)-SWNTs, respectively.

Received 14 January 2008; accepted 1 May 2008; published 30 May 2008.

References

- Dresselhaus, M. S., Dresselhaus, G. & Avouris, P. *Carbon Nanotubes: Synthesis, Structure, Properties and Applications* (Springer, Berlin, 2001).
- Papadimitrakopoulos, F. & Ju, S.-Y., Purity rolled up in a tube. *Nature* **450**, 486–487 (2007).
- Zheng, M. *et al.* DNA-assisted dispersion and separation of carbon nanotubes. *Nature Mater.* **2**, 338–342 (2003).
- Zheng, M. *et al.* Structure-based carbon nanotube sorting by sequence-dependent DNA assembly. *Science* **302**, 1545–1548 (2003).
- Nish, A., Hwang, J.-Y., Doig, J. & Nicholas, R. J., Highly selective dispersion of single-walled carbon nanotubes using aromatic polymers. *Nature Nanotech.* **2**, 640–646 (2007).
- Chen, F., Wang, B., Chen, Y. & Li, L.-J., Toward the extraction of single species of single-walled carbon nanotubes using fluorene-based polymers. *Nano Lett.* **7**, 3013–3017 (2007).
- Peng, X. *et al.*, Optically active single-walled carbon nanotubes. *Nature Nanotech.* **2**, 361–365 (2007).
- Chattopadhyay, D., Galeska, I. & Papadimitrakopoulos, F., A route for bulk separation of semiconducting from metallic single-wall carbon nanotubes. *J. Am. Chem. Soc.* **125**, 3370–3375 (2003).
- Kim, S. N., Luo, Z. & Papadimitrakopoulos, F., Diameter and metallicity dependent redox influences on the separation of single-wall carbon nanotubes. *Nano Lett.* **5**, 2500–2504 (2005).
- Krupke, R., Hennrich, F., Lohneysen, H. v. & Kappes, M. M., Separation of metallic from semiconducting single-walled carbon nanotubes. *Science* **301**, 344–347 (2003).
- Strano, M. S. *et al.*, Electronic structure control of single-walled carbon nanotube functionalization. *Science* **301**, 1519–1522 (2003).
- Arnold, M. S., Green, A. A., Hulvat, J. F., Stupp, S. I. & Hersam, M. C., Sorting carbon nanotubes by electronic structure using density differentiation. *Nature Nanotech.* **1**, 60–65 (2006).
- Zheng, M. & Semke, E. D., Enrichment of single chirality carbon nanotubes. *J. Am. Chem. Soc.* **129**, 6084–6085 (2007).
- Massey, V., The chemical and biological versatility of riboflavin. *Biochem. Soc. Trans.* **28**, 283–296 (2000).
- Guisseppi-Elie, A., Lei, C. & Baughman, R. H., Direct electron transfer of glucose oxidase on carbon nanotubes. *Nanotechnology* **13**, 559–564 (2002).
- Patolsky, F., Weizmann, Y. & Willner, I., Long-range electrical contacting of redox enzymes by SWCNT connectors. *Angew. Chem. Int. Ed.* **43**, 2113–2117 (2004).
- Lin, C. S., Zhang, R. Q., Niehaus, T. A. & Frauenheim, T., Geometric and electronic structures of carbon nanotubes adsorbed with flavin adenine dinucleotide: A theoretical study. *J. Phys. Chem. C* **111**, 4069–4073 (2007).
- Ju, S. Y. & Papadimitrakopoulos, F., Synthesis and redox behavior of flavin mononucleotide-functionalized single-walled carbon nanotubes. *J. Am. Chem. Soc.* **130**, 655–664 (2008).
- Bachilo, S. M. *et al.*, Structure-assigned optical spectra of single-walled carbon nanotubes. *Science* **298**, 2361–2366 (2002).
- Zheng, M. & Diner, B. A., Solution redox chemistry of carbon nanotubes. *J. Am. Chem. Soc.* **126**, 15490–15494 (2004).
- O’Connell, M. J., Eibergen, E. E. & Doorn, S. K., Chiral selectivity in the charge-transfer bleaching of single-walled carbon-nanotube spectra. *Nature Nanotech.* **4**, 412–418 (2005).
- Stryer, L. *Biochemistry* (W.H. Freeman & Company, New York, 1995).
- Utsumi, S. *et al.*, RBM band shift-evidenced dispersion mechanism of single-wall carbon nanotube bundles with NaDDBS. *J. Colloid Interface Sci.* **308**, 276 (2007).

24. Tao, F. & Bernasek, S. L., Understanding odd-even effects in organic self-assembled monolayers. *Chem. Rev.* **107**, 1408–1453 (2007).
25. Niyogi, S. *et al.*, Selective aggregation of single-walled carbon nanotubes via salt addition. *J. Am. Chem. Soc.* **129**, 1898–1899 (2007).
26. Chou, S. G. *et al.*, Phonon-assisted excitonic recombination channels observed in DNA-wrapped carbon nanotubes using photoluminescence spectroscopy. *Phys. Rev. Lett.* **94**, 127402 (2005).
27. Nikolaev, P. *et al.*, Gas-phase catalytic growth of single-walled carbon nanotubes from carbon monoxide. *Chem. Phys. Lett.* **313**, 91–97 (1999).
28. O'Connell, M. J. *et al.*, Band gap fluorescence from individual single-walled carbon nanotubes. *Science* **297**, 593–596 (2002).
29. Richard, C., Balavoine, F., Schultz, P., Ebbesen, T. W. & Mioskowski, C., Supramolecular self-assembly of lipid derivatives on carbon nanotubes. *Science* **300**, 775–778 (2003).
30. Oyama, Y. *et al.*, Photoluminescence intensity of single-wall carbon nanotubes. *Carbon* **44**, 873–879 (2006).

Supplementary Information accompanies this paper at www.nature.com/naturenanotechnology.

Acknowledgements

The authors wish to thank Z. Luo, W. Kopcha and C. Badalucco for their help and S. Daniels for valuable discussions. This work has been supported mainly by Air Force Office of Scientific Research (AFOSR) FA9550-06-1-0030, and in part by National Science Foundation (NSF)-Nanoscale Interdisciplinary Research Team (NIRT) DMI-0422724, Army Research Office (ARO)-DAAD-19-02-1-10381, National Institute of Health (NIH)-ES013557 and the U.S. Army Medical Research W81XWH-05-1-0539.

Author contributions

S.J. and F.P. conceived and designed the experiments. S.J. performed sample preparation along with PLE and UV-vis-NIR characterization. J.D. performed HRTEM analysis. S.J. and I.S. performed data analysis. S.J. and F.P. performed the molecular simulation. S.J. and F.P. co-wrote the paper.

Author information

Reprints and permission information is available online at <http://npg.nature.com/reprintsandpermissions/>. Correspondence and requests for materials should be addressed to F.P.

Selection of Carbon Nanotubes with Specific Chiralities using Helical Assemblies of Flavin Mononucleotide

Sang-Yong Ju[†], Jonathan Doll[†], Ity Sharma[‡], and Fotios Papadimitrakopoulos^{†,‡,}*

Contribution from the Nanomaterials Optoelectronics Laboratory (NOEL), Polymer Program[†],
Department of Chemistry[‡], Institute of Materials Science, University of Connecticut, Storrs,
Connecticut 06269-3136

* Correspondence E-mail: papadim@mail.ims.uconn.edu

Table of Contents.....	S1
Figure S1.....	S2
Figure S2.....	S3
Figure S3.....	S4
Figures S4-S5	S5
Figures S6-S7	S6
Tables S1 and S2	S7

Figure S1. Diameter vs. relative PL intensity of (a) starting SDBS-dispersed HiPco sample (fig. 1a), (b) FMN-dispersed HiPco sample (fig. 1b), and (c) after addition of 7.4 mM SDBS into the FMN-HiPco sample of (b) (fig. 1c).

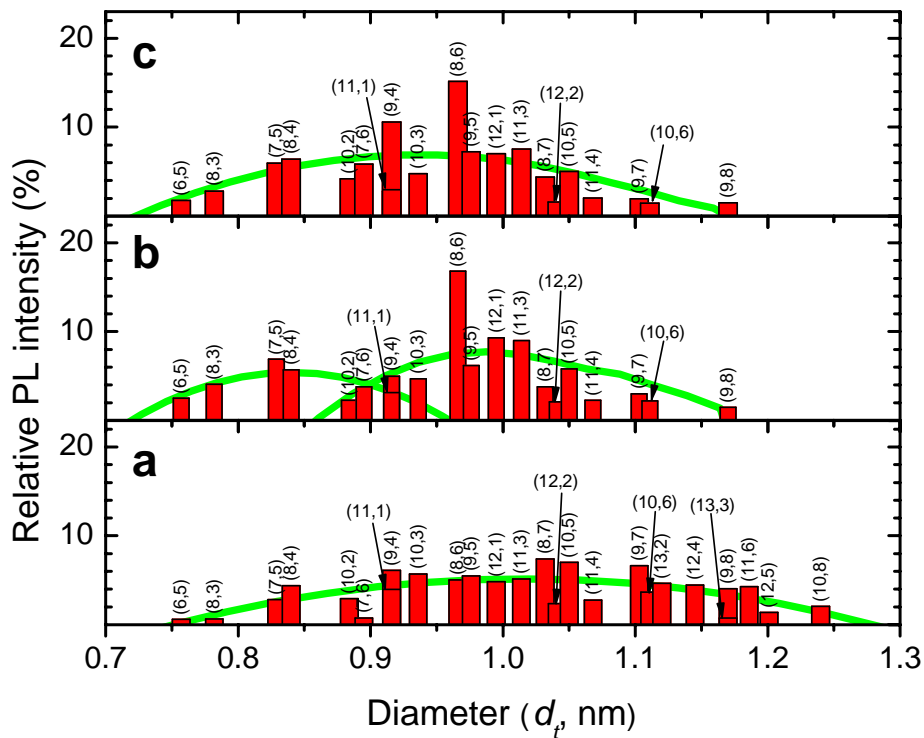


Figure S2. Additional HRTEM images of FMN-wrapped HiPco nanotube. Fig. 2d and 2e originate from Fig. S2e and S2f, respectively.

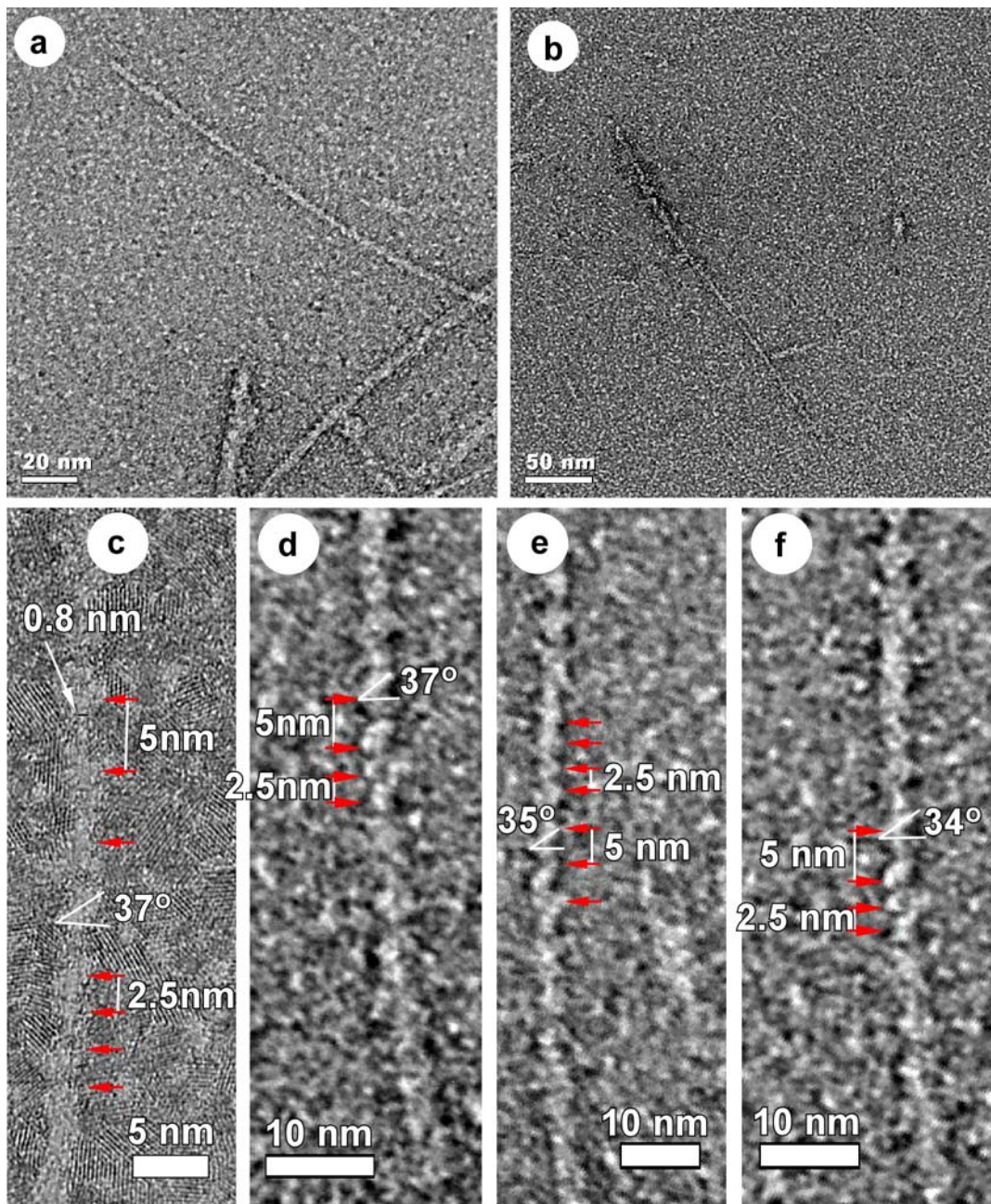


Figure. S3. Representative PLE maps of FMN-dispersed HiPco, containing different SDBS concentration of (a) 0.66 mM, (b) 1.32 mM, and (c) 2.32 mM.

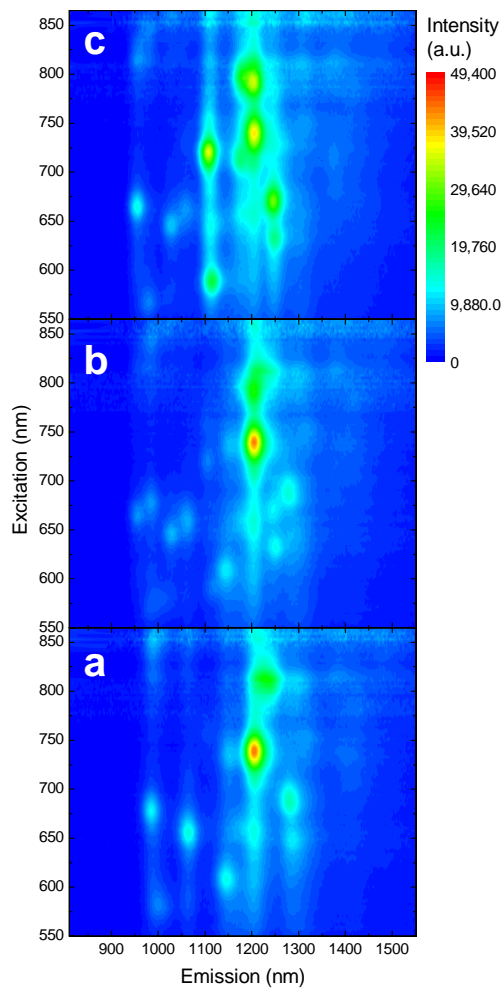


Figure S4. Chiral angle vs. E_{22}^S redshift for various chirality nanotubes. Zigzag lines follows a distinct colored-coded family ($2n+m=\text{constant}$) and modality ($\text{mod}[(n-m)/3] = 1$ or 2) patterns.

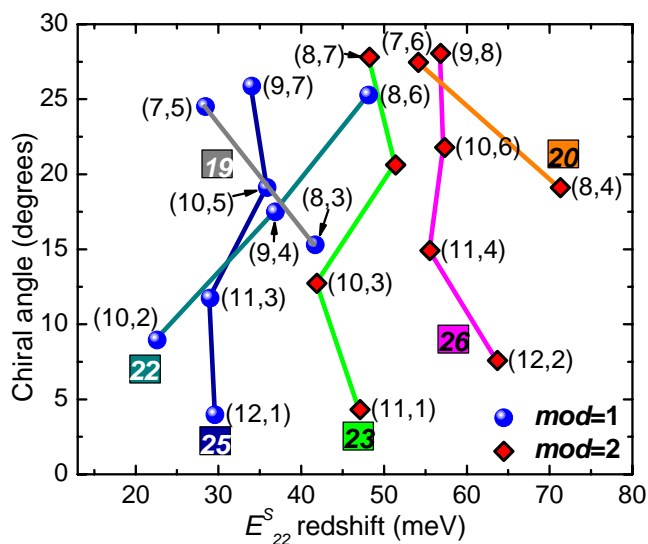


Figure S5. UV-Vis-NIR spectra of FMN-dispersed SWNTs against NaCl addition. No significant bundling or nanotube precipitation is witnessed for up to 0.714 M of NaCl.

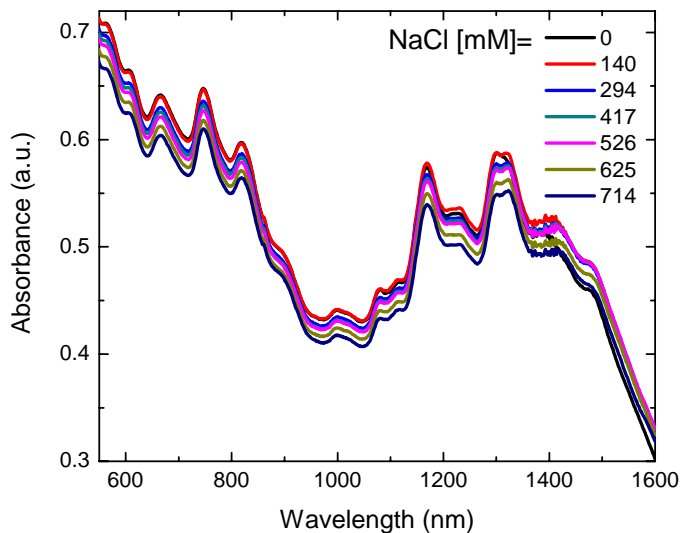


Figure S6. Baseline close-up of the PLE map of Fig. 6a.

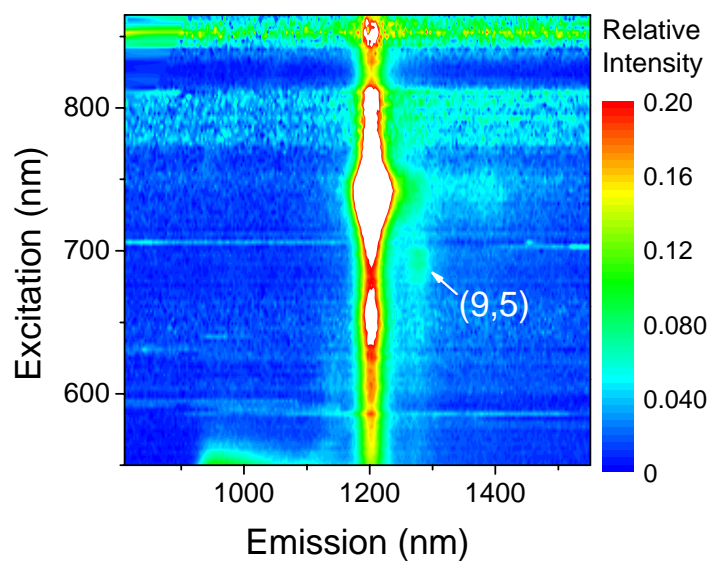


Figure S7. Deconvoluted NIR spectrum of Fig. 6b.

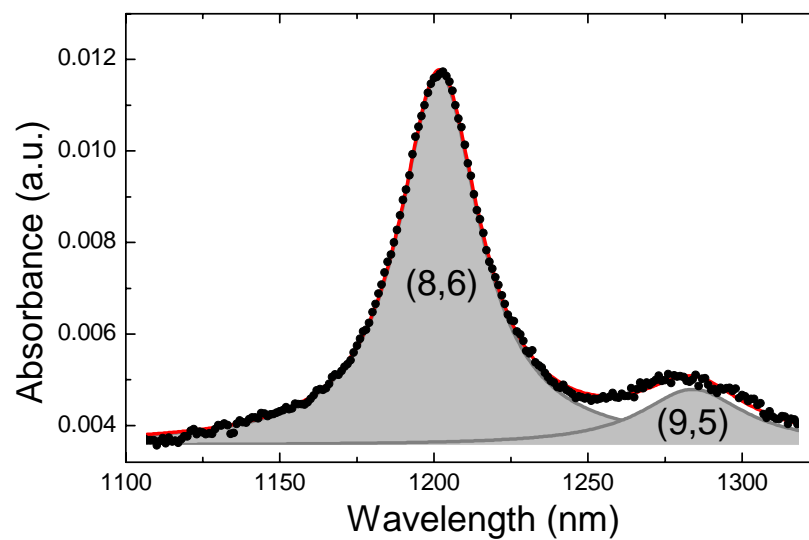


Table S1. E_{11}^S and E_{22}^S positions, FWHM, redshift, and % PL quenching from Samples a, b and c of Figs. 1a-c.

Assignment			SDBS-HiPco sample (a)					FMN-HiPco sample (b)					7.4 mM SDBS addition sample b (c)					Redshift [♣]		Difference in [♣]				Assignment
(n,m)	d_i	Chiral	E_{11}^S	E_{22}^S	FWHM	FWHM	Rel.	E_{11}^S	E_{22}^S	FWHM	FWHM	Rel.	E_{11}^S	E_{22}^S	FWHM	FWHM	Rel.	ΔE_{11}^S	ΔE_{22}^S	FWHM	FWHM	%PL [¥]	(n,m)	
Angle			of E_{11}^S			of E_{22}^S			of E_{11}^S			of E_{22}^S					of E_{11}^S		of E_{22}^S		quench			
nm	degrees		nm	nm	meV	meV	%	nm	nm	meV	meV	%	nm	nm	meV	meV	%	meV	meV	meV	meV	%		
(6,5)	0.76	27.0	974	569	72	118	0.6	1003	582	63	106	2.5	979	568	53	130	1.8	36	49	9	11	13	(6,5)	
(8,3)	0.78	15.3	952	663	66	93	0.6	986	678	59	78	4.1	955	665	55	71	2.8	44	42	7	16	9	(8,3)	
(7,5)	0.83	24.5	1025	646	53	82	2.8	1062	655	54	109	6.9	1028	645	45	83	6.0	42	28	-1	-27	28	(7,5)	
(8,4)	0.84	19.1	1114	587	45	102	4.4	1148	608	39	96	5.7	1116	589	36	102	6.4	32	71	6	6	45	(8,4)	
(10,2)	0.88	8.9	1054	736	46	69	2.9	1102	746	49	84	2.3	1058	735	40	68	4.2	51	23	-2	-15	66	(10,2)	
(7,6)	0.89	27.5	1121	647	41	85	0.8	1155	666	44	104	3.8	1120	647	36	86	5.9	32	54	-3	-18	60	(7,6)	
(11,1)	0.92	4.3	1263	611	42	116	4.0	1299	625	32	89	3.0	1263	610	35	95	2.8	27	47	10	27	34	(11,1)	
(9,4)	0.92	17.5	1105	721	38	94	6.1	1146	737	41	67	5.0	1106	720	35	73	10.6	40	37	-4	27	71	(9,4)	
(10,3)	0.94	12.7	1247	637	35	88	5.7	1285	651	29	86	4.7	1251	630	31	96	4.8	30	42	6	2	39	(10,3)	
(8,6)	0.97	25.3	1175	717	34	75	5.0	1208	737	46	67	16.8	1178	715	29	62	15.1	28	48	-12	8	31	(8,6)	
(9,5)	0.98	20.6	1247	669	37	100	5.5	1281	689	37	72	6.2	1248	671	32	83	7.2	27	51	0	29	47	(9,5)	
(12,1)	0.99	4.0	1172	796	31	58	4.9	1214	811	40	64	9.3	1174	795	45	58	7.0	37	30	-9	-6	18	(12,1)	
(11,3)	1.01	11.7	1195	793	32	65	5.1	1238	808	40	64	9.0	1195	793	44	62	7.5	36	29	-8	0	26	(11,3)	
(8,7)	1.03	27.8	1262	726	34	82	7.4	1310	747	32	66	3.8	1268	727	29	67	4.4	36	48	3	17	47	(8,7)	
(12,2)	1.04	7.6	1380	681	31	73	2.4	1403	706	29	59	2.1	1375	682	26	78	1.6	15	64	2	13	18	(12,2)	
(10,5)	1.05	19.1	1249	786	29	57	7.0	1292	805	42	58	5.8	1251	787	37	64	5.0	33	36	-12	-1	28	(10,5)	
(11,4)	1.07	14.9	1371	711	25	72	2.8	1401	735	29	50	2.3	1371	714	30	64	2.0	19	56	-4	22	30	(11,4)	
(9,7)	1.10	25.9	1321	790	26	64	6.6	1375	812	29	38	3.0	1322	788	30	47	1.9	45	43	-3	32	15	(9,7)	
(10,6)	1.11	21.8	1380	755	26	69	3.7	1410	782	30	41	2.2	1372	755	24	58	1.5	19	57	-4	27	9	(10,6)	
(13,2)	1.12	7.1	1308	859	33	55	4.6																(13,2)	
(12,4)	1.14	13.9	1341	855	34	52	4.5																(12,4)	
(9,8)	1.17	28.1	1413	807	27	57	4.1	1448	838	33	32	1.5	1414	810	23	65	1.5	21	57	-6	25	35	(9,8)	
(13,3)	1.17	10.2	1497	760	25	86	4.3																(13,3)	
(11,6)	1.19	20.4	1394	857	30	52	2.1																(11,6)	
(12,5)	1.20	16.6	1492	798	26	56	1.4																(12,5)	
(10,8)	1.24	26.3	1474	865	24	58	0.7																(10,8)	

♣: FMN-HiPco (sample b)-starting HiPco (sample a), ¥: % PL quenching obtained from $(1 - (\text{PL}_{\text{FMN-HiPco, sample b}} / \text{PL}_{\text{SDBS-addition, sample a}})) \times 100$.

Table S2. Tabulated PLE intensities from the SDBS PL position of various (n,m) nanotubes, as a function of SDBS addition in FMN-wrapped nanotubes. The relative affinity (K_a) of FMN-SWNT wrapping against SDBS concentration and fitted Hill coefficient (γ) are also presented.

Assignment (n,m)	Diameter nm	Chiral Ang. degrees	Measured Point		SDBS concentration (mM)								K_a	γ
			E_{11}^S	E_{22}^S	0	0.66	0.99	1.32	1.65	1.98	2.31	2.65		
(6,5)	0.76	27	974	568	2290	2480	2180	4120	5590	6070	6290	6270	1.35	9.0±1.7
(8,3)	0.78	15.3	954	664	1230	1120	961	7210	12600	13300	13700	13700	1.33	12.1±1.5
(7,5)	0.83	24.5	1029	646	4300	2710	2600	9540	9360	10300	9550	10100	1.2	11.8±7.3
(8,4)	0.84	19.1	1116	589	3690	3060	2440	5800	16300	21500	22700	23800	1.56	9.7±1.2
(7,6)	0.89	8.9	1119	646	4820	3270	3140	4750	9540	11400	12500	12700	1.67	5.7±2.4
(11,1)	0.92	27.5	1263	610	5530	5250	4970	6410	7560	7920	8180	8900	1.51	4.8±1.9
(9,4)	0.92	17.5	1107	721	4680	2880	2110	6340	29100	34700	36400	37100	1.51	13.8±1.9
(10,3)	0.94	25.3	1251	631	6330	5810	5620	13400	16700	17700	18600	18800	1.28	9.6±2.4
(8,6)	0.97	20.6	1179	715	8170	7380	7410	8980	11400	12600	19500	22500	2.81	8.6±3.4
(9,5)	0.98	4	1248	670	7170	6740	6440	12100	27200	29600	30000	30600	1.44	13.6±0.9
(12,1)	0.99	12.7	1173	796	5110	4570	4600	12000	18600	21100	23500	22800	1.4	7.5±1.2
(11,3)	1.01	11.7	1194	793	12100	11500	10800	22300	32200	32200	31200	32300	1.3	16.4±8.2
(8,7)	1.03	27.8	1269	727	9250	8300	7480	8370	10600	10800	11000	11100	2.08	3.0±5.2
(12,2)	1.04	7.6	1374	682	3860	3670	3510	4250	4670	5390	5690	5880	1.69	4.6±1.6
(11,4)	1.07	14.9	1371	715	3830	3350	3300	4810	5430	6060	6370	6570	1.49	5.6±2.1